nature energy

Article

https://doi.org/10.1038/s41560-023-01302-y

Understanding hydrogen electrocatalysis by probing the hydrogen-bond network of water at the electrified Pt–solution interface

Received: 26 September 2021

Accepted: 9 June 2023

Published online: 6 July 2023

Check for updates

Qiang Sun[1], Nicholas J. Oliveira[2], Soonho Kwon[3], Sergiy Tyukhtenko[4], Jason J. Guo[1,5], Nathalie Myrthil[1], Steven A. Lopez[1], Ian Kendrick[1], Sanjeev Mukerjee[1], Lu Ma[6], Steven N. Ehrlich[6], Jingkun Li[7] ✉, William A. Goddard III[3] ✉, Yushan Yan[2] ✉ & Qingying Jia[1,8] ✉

Rational construction of the electrode–solution interface where electrochemical processes occur is of paramount importance in electrochemistry. Efforts to gain better control and understanding of the interface have been hindered by lack of probing methods. Here we show that the hydrogen evolution and oxidation reactions (HER/HOR) catalysed by platinum in base can be promoted by introduction of *N*-methylimidazoles at the platinum–water interface. In situ spectroscopic characterization together with simulations indicate that the *N*-methylimidazoles facilitate diffusion of hydroxides across the interface by holding the second layer of water close to platinum surfaces, thereby promoting the HER/HOR. We thus propose that the HER/HOR kinetics of platinum in acid and base is governed by diffusion of protons and hydroxides, respectively, through the hydrogen-bond network of interfacial water by the Grotthuss mechanism. Moreover, we demonstrate a 40% performance improvement of an anion exchange membrane electrolyser by adding 1,2-dimethylimidazole into the alkali fed into its platinum cathode.

The pH has profound influences on the kinetics of electrochemical processes such as hydrogen electrocatalysis. The activity of the hydrogen evolution and oxidation reactions (HER/HOR) of several transition metals including platinum (Pt) progressively decreases as the pH increases[1–3]. The reason(s) behind this phenomenon has remained unclear despite decades of studies.

One primary strategy adopted in previous studies is to mix Pt with another metal such as Ni or Ru to improve its HER/HOR activity in alkali, followed by identifying the promoting roles of Ni/Ru (refs. 4–10). However, different groups proposed different promoting roles of Ni/Ru and suggested different causes for the sluggish HER/HOR of Pt in alkali. Some groups stated that the Ru/Ni improves the HER/HOR of Pt by weakening the binding energy between Pt and hydrogen (E_{PtH}) via strain and/or electronic effects, and ascribed the sluggish HER/HOR of Pt in base to the overly strong E_{PtH} (refs. 8–11). Other groups proposed that Ru/Ni promotes water

[1]Department of Chemistry and Chemical Biology, Northeastern University, Boston, MA, USA. [2]Center for Clean Hydrogen, Department of Chemical and Biomolecular Engineering, University of Delaware, Newark, DE, USA. [3]Liquid Sunlight Alliance (LiSA) and Materials and Process Simulation Center (MSC), California Institute of Technology, Pasadena, CA, USA. [4]Center for Drug Discovery and Departments of Pharmaceutical Sciences and Chemistry and Chemical Biology, Northeastern University, Boston, MA, USA. [5]Barnett Institute for Chemical and Biological Analysis, Northeastern University, Boston, MA, USA. [6]National Synchrotron Light Source II, Brookhaven National Laboratory, Upton, NY, USA. [7]School of Chemistry and Molecular Engineering, East China University of Science and Technology, Shanghai, China. [8]Present address: Plug Power Inc, Concord, MA, USA. ✉e-mail: lijingkun1987@gmail.com; wagoddard3@gmail.com; yanys@udel.edu; qjia@iit.edu

https://doi.org/10.1038/s41560-023-01302-y

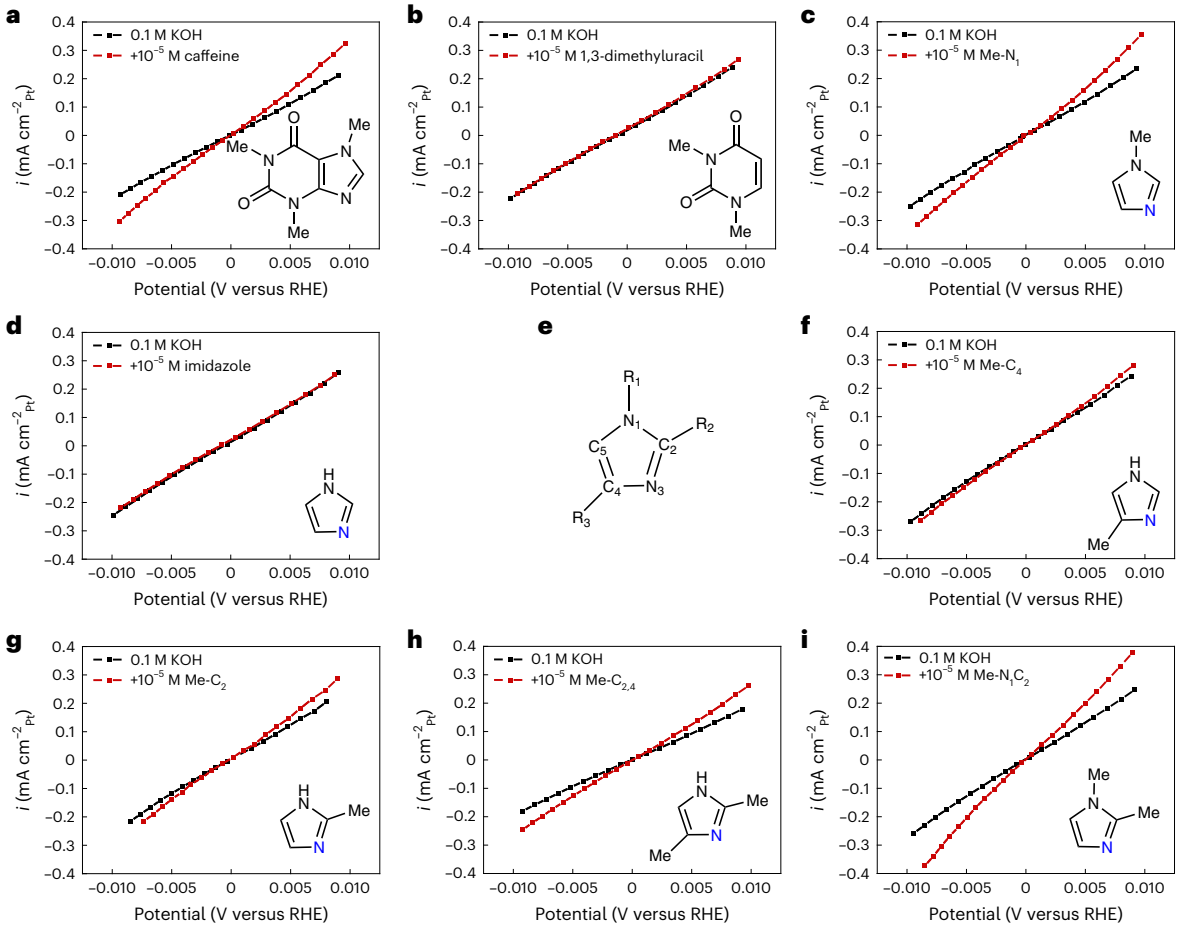

Fig. 1 | Structurally dependent promotion effects of organic compounds on the HOR/HER of Pt. a–**d**,**f**–**i**, The iR (i, current; R, resistance)-corrected HOR/HER low-overpotential kinetic current density of Pt/C (8 μg_{Pt} cm^{-2}) with or without 10^{-5} M caffeine (**a**), 1,3-dimethyluracil (**b**), imidazole (**d**) and *N*-methylimidazoles (**c**,**f**–**i**) in H_2-saturated 0.1 M KOH with a rotation rate of 2,500 r.p.m. and a scan rate of 20 mV s^{-1}, room temperature. The structure of the corresponding compound is given in the inset. **e**, The atomic numbering of the imidazole ring, with $R_{1,2,3}$ representing possible location(s) for methyl group(s) in *N*-methylimidazoles. Full polarization curves are given in Supplementary Fig. 1.

dissociation/formation owing to its high oxophilicity and attributed the sluggish HER/HOR of Pt in base to the high energy barriers of water dissociation/formation[4,6,7]. Another group showed that the Ni deposited on Pt surfaces negatively shifts the potential of zero free charge, which eases the flip of interfacial water, and in turn promotes the HER/HOR of Pt (refs. 12–14). They accordingly attributed the pH dependence of the HER/HOR activity of Pt to the pH-dependent potential of zero free charge[15,16]. We recently identified the promoting role of Ru as facilitating interfacial water shuffling of the HER/HOR intermediates[17]. Because of the ambiguity over the promoting roles of Ni/Ru, this strategy has not led to a conclusive explanation of the sluggish HER/HOR kinetics of Pt in alkali. Finding other promoters with definitive promoting roles may give definitive answers to this open question and provide alternative routes to promote the HER/HOR of Pt in alkali.

It was recently found that adding caffeine into alkaline solution substantially improved the HER/HOR activity of Pt, but the mechanism for this improvement was unclear[18]. This work inspired us to seek other organic compounds that promote HER/HOR of Pt in base and then to identify their promoting roles to understand the HER/HOR kinetics of Pt. In this Article, by studying a set of *N*-methylimidazoles via a combination of rotating disk electrode (RDE), nuclear magnetic resonance (NMR) and quantum mechanics computations, we found that the more negatively charged pyridinic nitrogen (N_3) of *N*-methylimidazole forms a stronger hydrogen bond (H-bond) with interfacial H_2O and gives greater improvements of the HER/HOR rate of Pt. In situ attenuated total reflectance surface-enhanced infra-red reflection absorption spectroscopy (ATR-SEIRAS) coupled with surface-enhanced Raman and ab initio molecular dynamics (AIMD) showed that 1,2-dimethylimidazole forms a strong $N_3\cdots H_2O$ bond with interfacial water. These findings enabled us to identify the promoting role of *N*-methylimidazoles in facilitating the Volmer step of Pt in alkali.

N-methylimidazoles promote the HER/HOR of Pt

We first verified that adding 10^{-5} M caffeine into 0.1 M KOH electrolyte markedly improved the HER/HOR activity of Pt/C (TKK, 47.7 wt%) (Fig. 1a) in an RDE as previously reported[18]. We then tested 10^{-5} M 1,3-dimethyluracil and 1-methylimidazole (Me-N_1), the left and right parts of the caffeine molecule depicted in Fig. 1a inset, respectively, to determine which part(s) of caffeine contribute to the improvement. The 1,3-dimethyluracil did not promote the HER/HOR of Pt (Fig. 1b), whereas 1-methylimidazole did (Fig. 1c). Following this observation, we added a set of *N*-methylimidazoles with different numbers of methyl groups (-CH_3) located at different positions of the imidazole ring (Fig. 1d–i) into 0.1 M KOH to promote the HER/HOR of Pt/C, which renders delicate tailoring of the molecular structure of the probes. These compounds are accordingly labelled by the locations of methyl groups hereafter (a list of the notions given in Supplementary Table 1). We quantified their improvements of the HER/HOR specific

https://doi.org/10.1038/s41560-023-01302-y

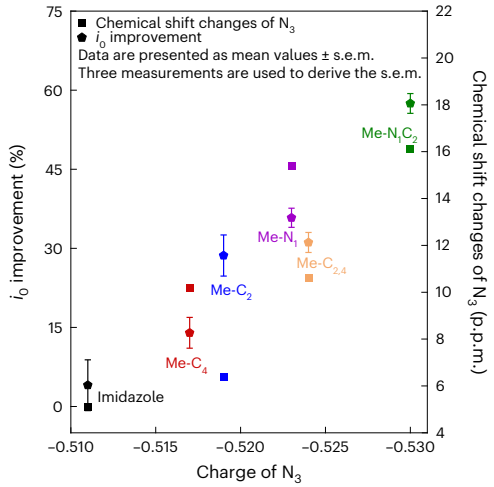

Fig. 2 | *N*-methylimidazoles promote the HOR/HER of Pt through the N_3···H_2O bonding. The i_0 improvements (left *y* axis) and the $^{14}N_3/^{15}N_3$ chemical shift changes (right *y* axis) of *N*-methylimidazoles between two different media as a function of the charge of their N_3(s). The charges of the N_3 were determined by DFT, with the rapid averaging of the N_1 and N_3 charge via proton exchange[20] taken under consideration for imidazole, Me-C_2, Me-C_4 and Me-$C_{2,4}$ (Supplementary Note 1). The $^{14}N_3/^{15}N_3$ chemical shift changes were obtained by subtracting the resonance peak position in 10% CD_2Cl_2 + 90% CH_2Cl_2 from that in 0.1 M KOH with 10% D_2O + 90% H_2O (NMR spectra given in Supplementary Fig. 5). The error bars were generated from the standard error of the mean (s.e.m.) derived from three measurements.

exchange current densities (i_0) of Pt/C by fitting the kinetic currents to the Butler–Volmer equation (Methods). The electrochemical surface area was derived from the hydrogen underpotential deposition (H_{upd}) charge of the cyclic voltammetry (CV) of Pt/C in 0.1 M KOH within the potential range of 0.05–0.45 V (versus reversible hydrogen electrode (RHE)).

The average i_0 of Pt/C in these cases is 0.64 ± 0.02 mA cm_{Pt}^{-2}, comparable to that (0.57 ± 0.07 mA cm_{Pt}^{-2}) of Pt/C reported previously[19] under similar conditions. Although the H_{upd} charge of Pt/C was substantially suppressed by the *N*-methylimidazoles (Supplementary Fig. 2), probably via the steric effect, the HOR limiting current density remained unchanged for all cases. Moreover, the HER/HOR polarization curves overlapped with or without adding 10^{-5} M imidazole or 1,3-dimethyluracil (Supplementary Fig. 3). These phenomena indicate that these *N*-methylimidazoles do not block the Pt sites for the HER/HOR as spectators. We therefore used the H_{upd} charge of Pt/C obtained in the 0.1 M KOH electrolyte before addition of *N*-methylimidazoles as the electrochemical surface area of the Pt/C in 0.1 M KOH with *N*-methylimidazoles. Higher concentrations of 10^{-4} M and 10^{-3} M were found to give similar improvement as 10^{-5} M (Supplementary Fig. 4).

In general, the *N*-methylimidazoles with more -CH_3(s) give higher i_0 improvements (Fig. 2 and Supplementary Table 1). No significant improvement was observed for imidazole that contains no -CH_3 (5 ± 5%). As the number of -CH_3 increases, the i_0 improvement generally increases until reaching 57 ± 2% for Me-N_1C_2 that contains two -CH_3(s). The position of -CH_3 also affects the improvement. The improvement of Me-N_1 (36 ± 2%) with the -CH_3 bonded with N_1 is higher than those of Me-C_4 (14 ± 3%) and Me-C_2 (28 ± 4%). Similarly, the improvement of Me-N_1C_2 (57 ± 2%) is higher than that of Me-$C_{2,4}$ (33 ± 2%). By contrast, 1,3-dimethyluracil with the two -CH_3(s) bonded with N_1 and N_3 does not improve the i_0 of Pt/C (Fig. 1b), which suggests that -CH_3 alone does not promote the HER/HOR of Pt/C. Therefore, a wide range of i_0 improvements was achieved by varying the position and/or number of -CH_3 in the *N*-methylimidazoles.

N-methylimidazoles interact with interfacial water

To identify the roles of -CH_3, we used density functional theory (DFT) calculations to determine the partial charges of these *N*-methylimidazoles. We found that the i_0 improvement of these *N*-methylimidazoles increases monotonously with the negative charge of N_3 (Fig. 2), and the negative charge of N_3 is affected by the number and position of -CH_3 (Supplementary Table 2), a well-known electron-donating group. These results suggest that the -CH_3(s) affect the *N*-methylimidazoles-induced HER/HOR activity improvement of Pt through tuning the charge of N_3.

To elucidate the catalytic role of N_3, we conducted ^{14}N and ^{15}N NMR experiments on these *N*-methylimidazoles in 0.1 M KOH as well as in CH_2Cl_2 solution as a baseline because the N atoms in *N*-methylimidazoles have minimal interactions with CH_2Cl_2 (ref. 20). When transferring from 0.1 M KOH to CH_2Cl_2 solution, the $^{14}N_3$ chemical shifts of Me-N_1 and Me-N_1C_2 exhibit a downfield shift of 15.4 and 16.1 p.p.m., respectively (details given in Supplementary Note 2). A comparable shift (15 p.p.m.) was previously reported[20] by transferring Me-N_1 from 0.1 M KOH to CH_2Cl_2 and ascribed to the change of the bonding from N_3···H_2O to N_3. This change verifies the interaction between the lone-pair electrons of the N_3 and the H of the H_2O (N_3···H_2O bond), which has been widely observed in *N*-methylimidazole solvent[21]. Combining the DFT and NMR with RDE results leads to the trend that Me-N_1C_2 exhibits a more negative N_3, stronger N_3···H_2O bond, and higher i_0 improvement than Me-N_1 (Fig. 2). The same trend is also observed between imidazole and Me-C_2 and between Me-C_4 and Me-$C_{2,4}$ (Fig. 2 and Supplementary Table 1–3), with the only difference in each couple being an additional -CH_3 bonded with C_2. This trend indicates that the -CH_3(s) in the *N*-methylimidazoles tune the negative charge of N_3 and in turn the N_3···H_2O bond strength, thereby modulating the i_0 improvement. We infer from these results that the *N*-methylimidazoles promote the HER/HOR of Pt in 0.1 M KOH by the N_3···H_2O bonding.

In situ ATR-SEIRAS was then conducted to probe the effects of *N*-methylimidazoles on the interfacial water structure near Pt surfaces during the HER/HOR. Spectra were collected during potential steps in an H_2-saturated 0.1 M KOH solution with and without 10^{-5} M Me-N_1C_2. For both cases, the spectra collected at 0.5 V (double-layer region) were used as a baseline for subtraction. The characteristic features of interfacial water, two ν(OH) bands at ~3,500 and ~3,000 cm^{-1} (Fig. 3a) and a δ(HOH) band at ~1,610 cm^{-1} (Supplementary Fig. 6)[22–24], were observed in the spectra collected in 0.1 M KOH free of Me-N_1C_2 within the H_{upd} potential region. It has been established that water monomers possess ν(OH) bands around 3,700 cm^{-1}, and the H-bond among water molecules red-shifts and broadens the ν(OH) bands substantially for hydrogen donors but modestly for hydrogen acceptors[22,23]. Therefore, the broad band around 3,000 cm^{-1} is characteristic of the strongly hydrogen-bonded water structure composed of hydrogen donors close to the Pt surface, whereas the sharp band around 3,500 cm^{-1} arises from the weakly hydrogen-bonding water structure made of hydrogen acceptors[22]. Consistent with previous studies[22,24], the intensity of the ν(OH) band around 3,000 cm^{-1} progressively decreases as the potential reduces from 0.5 V to 0 V, accompanied by a slight growth of the ν(OH) band between 3,300 cm^{-1} and 3,500 cm^{-1}, and both bands blue-shift (Fig. 3a). These spectral changes have been ascribed to the potential-dependent re-orientation of the H-up water (H_2O(H-up), proton donor) towards H-down water (H_2O(H-down), proton acceptor)[22,23]. This potential-dependent re-orientation of interfacial water has also been observed by in situ Raman[25] and in situ X-ray diffraction[26], and rationalized by computations that Pt surfaces become more negatively charged with reducing potential (versus RHE) and thus favour bonding with H_2O(H-down) over H_2O(H-up)[27]. However, the general trends of the ν(OH) bands are dramatically altered upon addition of 10^{-5} M Me-N_1C_2 into 0.1 M KOH. The 3,000 cm^{-1} band undergoes neither a decrease in intensity nor a blue shift with potential (Fig. 3b), indicative of Me-N_1C_2 retaining the strong H-bond interfacial water near the Pt surface.

https://doi.org/10.1038/s41560-023-01302-y

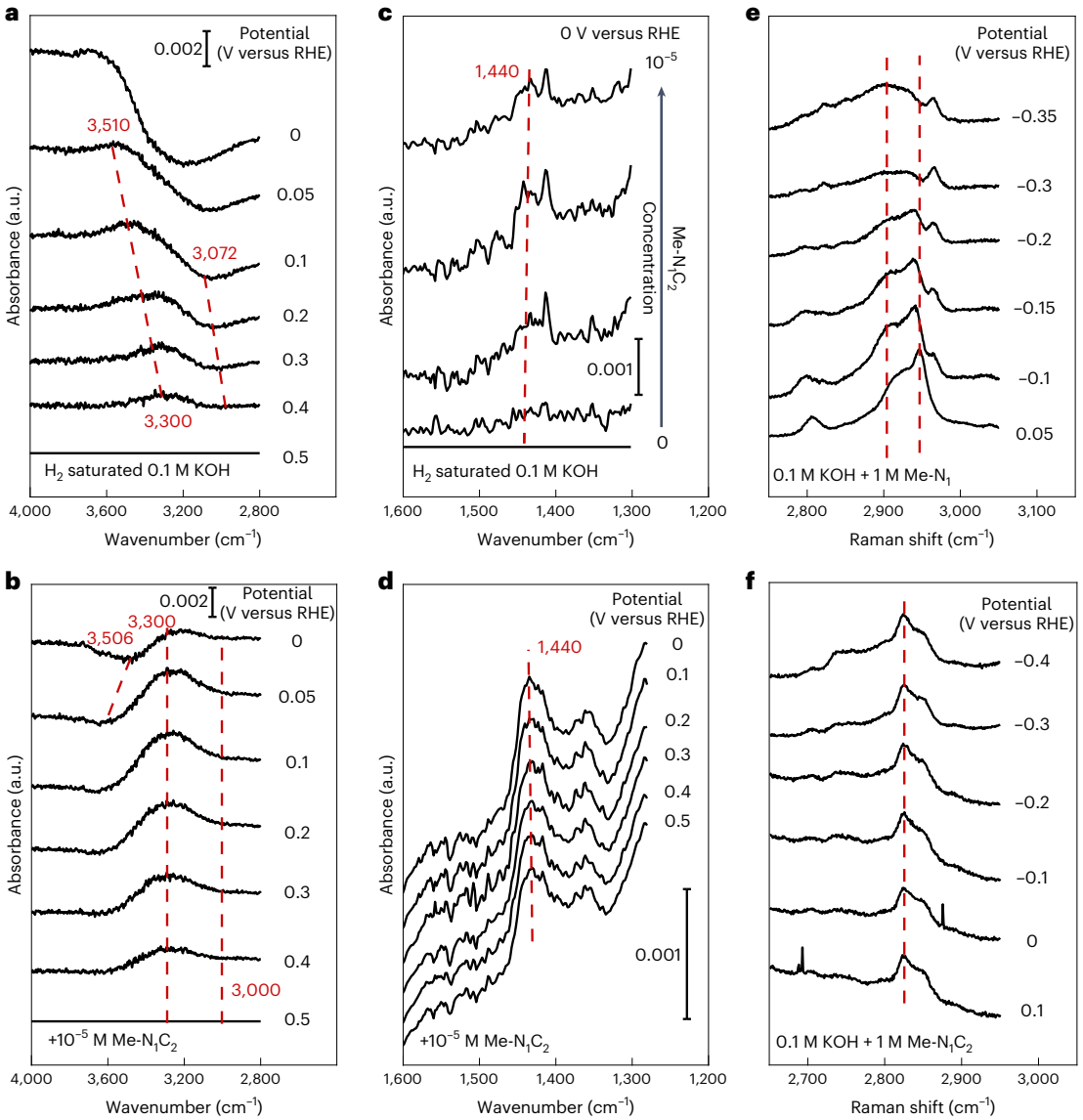

Fig. 3 | In situ probe of interfacial water and *N*-dimethylimidazoles. a,**b**, The in situ ATR-SEIRAS spectra of interfacial water on a Pt film collected in 0.1 M KOH without (**a**) and with (**b**) 10^{-5} M Me-N_1C_2. **c**, The in situ ATR-SEIRAS spectra of Me-N_1C_2 collected in 0.1 M KOH at 0 V with increasing concentration. **d**, The in situ ATR-SEIRAS spectra of Me-N_1C_2 with a concentration of 10^{-5} M in 0.1 M KOH at various potentials. **e**,**f**, The in situ Raman spectra were collected in 0.1 M KOH with 1 M Me-N_1 (**e**) and Me-N_1C_2 (**f**) on an Ag electrode.

In situ ATR-SEIRAS also provided information of the binding configuration of the interfacial Me-N_1C_2. The peak at 1,440 cm^{-1}, which was identified as the C-H bending mode of the -CH_3 (ref. 28), gradually grows upon the addition of Me-N_1C_2 into 0.1 M KOH when holding at 0 V (Fig. 3c), which is clearly reflected by the subtractive spectra (Supplementary Fig. 7). The lack of a shift of this peak with changing potential (Fig. 3d) indicates the lack of stark effects of the -CH_3(s) and thus the lack of chemical bonding with the Pt surface[29]. This is further confirmed by X-ray absorption spectroscopy (XAS) from the Pt perspective. The XAS spectrum at the Pt L_3-edge remains unchanged upon adding 10^{-5} M Me-N_1C_2 onto the Pt XAS electrode despite the suppressed H_{upd} peaks (Supplementary Fig. 8), which suggests that the bonding between Me-N_1C_2 and Pt is not sufficiently strong or abundant to be detectable by the XAS, given that specific adsorption of H (ref. 30) and CO (refs. 31,32) on Pt/C change the Pt XAS spectrum markedly.

In situ Raman was implemented to probe the orientation of *N*-methylimidazoles near the silver (Ag) electrode in 0.1 M KOH, given that the feasibility of this method was demonstrated previously thanks to the enhancement effect of Ag on Raman signals[33]. The in situ Raman spectra of Me-N_1 exhibit two sets of dynamic peaks within 2,800–3,200 cm^{-1} in the potential range of −0.35 to −0.05 V (Supplementary Fig. 9a), matching well with those of Me-N_1 previously reported in 0.1 M KCl (ref. 33). The growth and broadening of the $\nu(CH_3)$ bands between 2,850 cm^{-1} and 2,950 cm^{-1} with reducing potential observed here (Fig. 3e) were previously reported[33] and ascribed to the potential dependent re-orientation of Me-N_1. Specifically, the Me-N_1 interacts with the positively charged surface through the N_3 lone pair electrons at high potentials, while the -CH_3 points away from the surface, making the ring plane nearly normal to the surface. At low potentials, the positive -CH_3 prefers to interact with the negatively charged surface via field-induced dipole interactions, rendering the ring largely parallel to the surface[33,34]. By contrast, the $\nu(CH_3)$ bands of Me-N_1C_2 are largely preserved within the potential range of −0.4 to −0.1 V (Fig. 3f). The same phenomenon was previously observed on Me-C_2 and explained as -CH_3 bonded with the C_2 next to N_3, so it remains close to the surface even when the positively charged surface interacts with N_3 and inhibits[33].

The divergent Raman results between Me-N_1 and Me-N_1C_2 indicates that the -CH_3 bonded with the C_2 upholds the parallel configuration of the imidazole ring, which implicates a beneficial spatial effect of the -CH_3, in addition to modulating the charge of N_3. The spatial effect of -CH_3 found on the Ag surface shall be applicable to Pt surfaces despite possibly different ring-re-orientation potentials given that our in situ ATR-SEIRAS showed the -CH_3 not forming chemical bonding with the Pt surfaces, which is further confirmed by AIMD as shown next.

N-methylimidazoles facilitate hydroxide diffusion

To further examine the roles of Me-N_1C_2, we conducted AIMD simulations on the Pt(100)–water interface with and without Me-N_1C_2 in the explicit solvent (details given in Supplementary Note 3). Following our previous work using a hybrid scheme that combined implicit and explicit solvation[35], we chose a net electron charge of 0 e^- and 3 e^- as the surface charge of Pt to represent the 0 V versus RHE in the acidic and alkaline media, respectively. The Pt(100)–water interface was first constructed without Me-N_1C_2 as a baseline. In the alkali, all the water molecules in the first layer (closest to the surface) have the H-down orientation (H_2O(H-down)^{1st}) (Fig. 4a), owing to the interaction between the negatively charged surface and the dipole of O–H bonds. This is further manifested by the O distribution of the H_2O(H-down)^{1st} along the axis perpendicular to the surface that gives an average distance of 3.14 Å (Fig. 4b). The H_2O(H-down)^{1st} molecules (H-bond acceptors) form H-bonds with the H_2O(H-down)^{2nd} molecules (H-bond donors), thereby constructing the interfacial H-bond network (Fig. 4a).

We then introduced Me-N_1C_2 into the Pt(100)–water interface with three binding configurations (Supplementary Fig. 10). Among them, the imidazole-ring binding in parallel to the surface (Fig. 4c) with the Pt–C and Pt–N bond distances within a narrow range of 2.1 ± 0.1 Å and the non-chemical Pt-CH_3 bonds ≥2.9 Å (Supplementary Table 4) is the most energetically favourable configuration, in agreement with our in situ ATR-SEIRAS and Raman results (Supplementary Note 3). In this configuration, the H_2O(H-down)^{2nd} is an H-bond donor to both the H_2O(H-down)^{1st} (Fig. 4c) and the N_3 of Me-N_1C_2, the latter in line with our NMR results.

We then carried out metadynamics simulations[36] to examine how the Me-N_1C_2 affects the Volmer step ($H_2O + e^- \rightarrow H_{ad} + OH^-$) that has been acknowledged as the rate-determining step of the HER of Pt in alkali[3,19]. In the absence of Me-N_1C_2, as a biased potential is applied, the Volmer step occurs around 920 fs as indicated by the substantial elongation of the O–H bond ('a' in Fig. 4d) in the H_2O(H-down)^{1st} (Fig. 4e). This step is triggered by the specific adsorption of the H_2O(H-down)^{1st} (H_2O_{ad}(H-down)) as reflected by the abrupt shortening of the Pt–H bond distance to ~1.5 Å ('1' in Fig. 4e). Upon the H_2O_{ad}(H-down) dissociation, the H_2O_{ad}(H-down)-Pt bond shortens from 2.74 Å to 1.91 Å ('2' in Fig. 4e), which indicates that the generated hydroxide moves towards the Pt surface and becomes chemisorbed (OH_{ad}). The atomic trajectory of this process is provided in Supplementary Video 1. Its kinetic barrier is estimated as 0.82 eV (detailed calculations given in Methods).

With the presence of Me-N_1C_2, once a hydroxide is generated from the H_2O_{ad}(H-down) dissociation at around 650 fs, the H_2O(H-down)^{2nd} bonded with the Me-N_1C_2 (the left sphere water molecule in Fig. 4c) immediately transfers its proton to the hydroxide before it adsorbs to the surface, thereby replenishing the H_2O(H-down)^{1st} (the right sphere water molecule in Fig. 4c), as reflected by the shortening of the H-bond between them ('b' in Fig. 4f). Then, the OH^- diffuses into bulk solution through the Grotthuss mechanism with about 50 fs for each proton hopping[37,38] (Supplementary Video 2), in contrast to the case absent of Me-N_1C_2. The barrier of this process is calculated as 0.28 eV, much lower than that without Me-N_1C_2. These results indicate that Me-N_1C_2 greatly lowers the energy barrier of the Volmer step of Pt in base and facilitates the diffusion of OH^- across the interface via the Grotthuss mechanism. Experimentally, we found adding 10^{-5} M *N*-methylimidazoles into 0.1 M KOH substantially delays the CO oxidation on Pt/C (Supplementary Fig. 12). This observation indicates that *N*-methylimidazoles impede specific adsorption of hydroxides, in line with our metadynamics simulations.

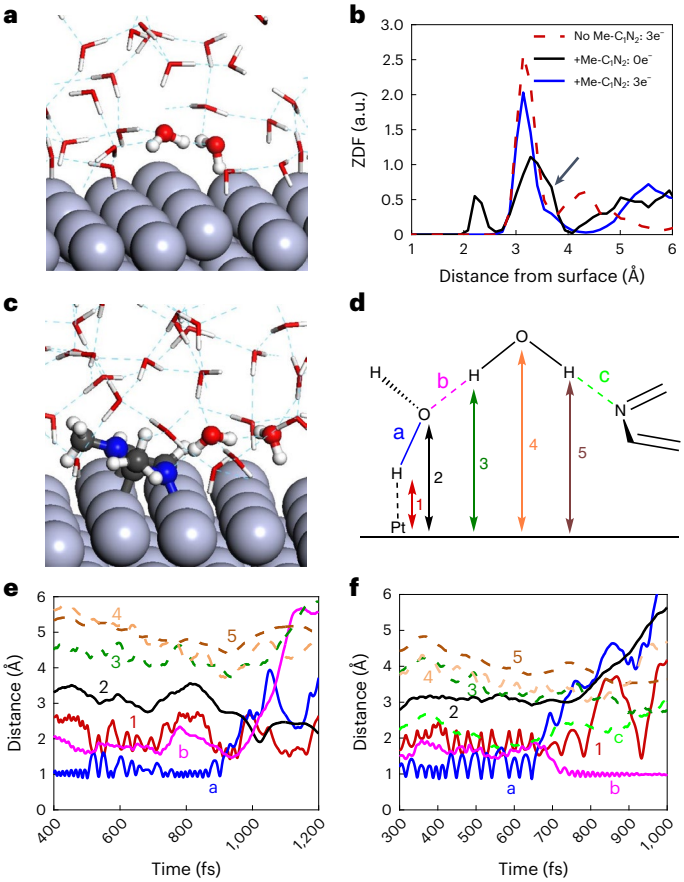

Fig. 4 | The Volmer step at the H_2O–Pt(100) interface with/without Me-N_1C_2. **a**, Atomic configuration of an equilibrated H_2O–Pt(100) interface at 300 K at 0 V versus RHE in alkali. The full scale is given in Supplementary Fig. 11a. **b**, Axial distribution function of water perpendicular to the surface along *z* axis (ZDF). Blue and red lines denote the H_2O–Pt(100) system with and without Me-N_1C_2, respectively. The black line indicates the acidic condition in presence of Me-N_1C_2. The arrow highlights the H_2O^{2nd} bonded with the H_2O(H-up)^{1st}. **c**, Atomic configuration of an equilibrated H_2O–Me-N_1C_2–Pt(100) interface at 300 K in alkali. The full scale is given in Supplementary Fig. 11b. **d**, Schematic illustration of an interfacial water dimer composed of an H_2O(H-down)^{1st} and H_2O(H-down)^{2nd} bonded with the N_3 of Me-N_1C_2. The numbers and letters represent the distance of atoms from Pt surface and the distances between atoms, respectively. The corresponding water dimer in **a** and **c** is represented by spheres. **e**,**f**, The time evolution of the bond distances during the Volmer step at the H_2O–Pt(100) interface with (**e**) and without (**f**) Me-N_1C_2 in alkali. The grey, brown, blue, red and white spheres in **a** and **c** represent Pt, C, N, O and H atoms, respectively.

The key difference between the Volmer steps with and without Me-N_1C_2 is that the H_2O(H-down)^{2nd} bonded with the Me-N_1C_2 donates a proton to the H_2O_{ad}(H-down) whereas the H_2O(H-down)^{2nd} in pure water does not. We postulate this difference is ascribable to Me-N_1C_2 holding the H_2O(H-down)^{2nd} much closer to the Pt surface (3.68 Å; '4' in Fig. 4f) via the $N_3\cdots H_2O$ bonding than the H_2O(H-down)^{1st} via the H-bond (4.34 Å; '4' in Fig. 4e). This can be rationalized by the N_3 being much closer to the Pt surface (2.08 Å) than the O of the H_2O(H-down)^{1st} (3.14 Å). The lowering of the H_2O(H-down)^{2nd} persists during the Volmer step (Fig. 4e,f), which facilitates the OH^- diffusion through it, thereby promoting the HER/HOR of Pt. The strong $N_3\cdots H_2O$ bonding holds the H_2O(H-down)^{2nd} close to Pt surfaces, which we speculate is indirectly

https://doi.org/10.1038/s41560-023-01302-y

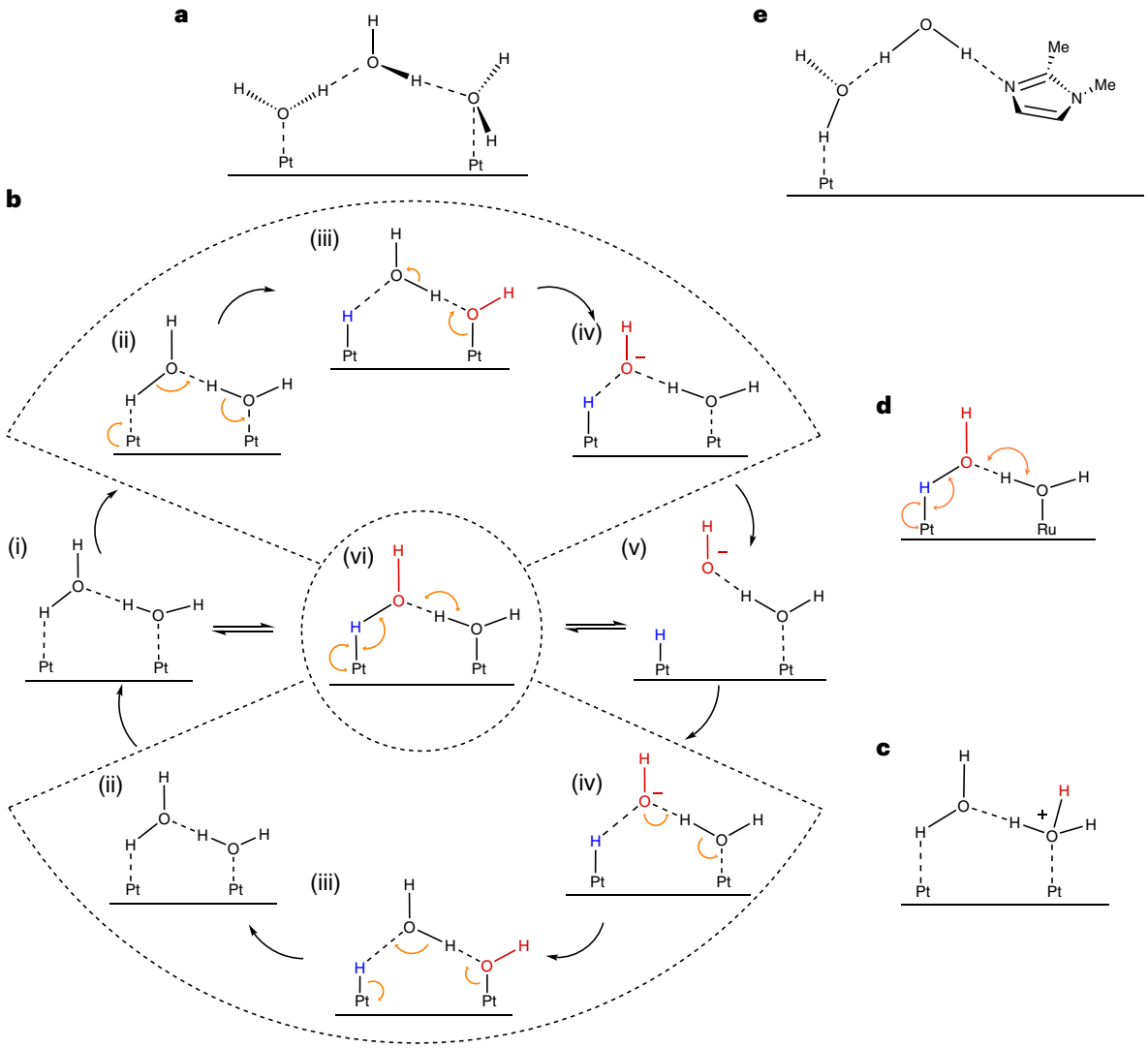

Fig. 5 | Proposed mechanisms for the Volmer process on Pt surfaces. **a**, Schematic drawing of a classic bilayer structure of water at the Pt surface, deduced from AIMD calculations. **b**, The elementary steps of the Volmer process of Pt surfaces in base, by which the water molecule specifically adsorbs onto Pt surfaces, triggering PCET to donate a proton to the Pt surface coupled with an electron donation from the Pt surface, which is accompanied by the transfer of a proton from neighbouring water, leading to the formation of an H_2O_{qad}(H-up) (in the dashed circle) through an H_{ad} (blue) and a hydroxide (red) above. **c**, Schematic drawing of a classic bilayer structure of water at the interface between the acidic solution and Pt surface. **d**,**e**, Surface Ru stabilizes H_2O(H-up)^{1st} (**d**) and Me-N_1C_2 stabilizes the H_2O(H-up)^{2nd} (**e**) on the Pt surface. The orange arrows represent the direction of electron transfer. Solid and dashed lines represent the covalent and non-covalent bonds, respectively. The different number of dashes indicates different bond lengths. Here a solid wedge indicates this bond or group is projecting out towards the viewer; a broken (hashed) wedge indicates this bond or group is receding away from the viewer. The ring in **e** is therefore parallel to the Pt surface.

affected by -CH_3(s) via modulating the charge of the N_3 and orientation of the imidazole ring.

The HER/HOR processes on Pt

While only the H_2O(H-down) is present in the first water layer on the Pt(100) surface in alkali, both H_2O(H-up)^{1st} and H_2O(H-down)^{1st} are present on the Pt(100) surface in acid (Supplementary Fig. 13). According to the calculated vibrational density of states of the water molecules using the 2PT analysis[39], the H_2O(H-up)^{1st} has shorter wavenumbers for O-H stretching than the H_2O(H-down)^{1st} (Supplementary Fig. 14), consistent with experimental data[22,23]. These results, in combination with the blue shift of the ATR-SEIRAS spectra with reducing potentials observed in the 0.1 M KOH free of Me-N_1C_2 (Fig. 3a), support the re-orientation from H_2O(H-up)^{1st} to H_2O(H-down)^{1st} with the increasing interfacial electric field (IEF). The O–H stretching wavenumbers of the H_2O(H-down)^{2nd} bonded with Me-N_1C_2 are lower than those of the H_2O(H-down)^{2nd} and comparable to those of the H_2O(H-up)^{1st} (Supplementary Fig. 14). This result suggests that the absence of the shift in the ATR-SEIRAS spectra with potential observed with Me-N_1C_2 in solution (Fig. 3b) can be ascribed to the strong N_3···H_2O bonding.

The average H_2O(H-up)^{1st}-Pt distance is 2.21 Å, much shorter than the H_2O(H-down)^{1st}–Pt distance (3.14 Å) (Fig. 4b) but comparable to the Pt–N_3 bond distance (2.08 Å). Consequently, the H_2O(H-down)^{2nd} forming H-bonding with this H_2O(H-up)^{1st} has an average H_2O(H-down)^{2nd}–Pt distance of 3.54 Å, much shorter than that of the H_2O(H-down)^{2nd} without Me-N_1C_2 (4.34 Å) in alkali but comparable to that (3.68 Å) of the

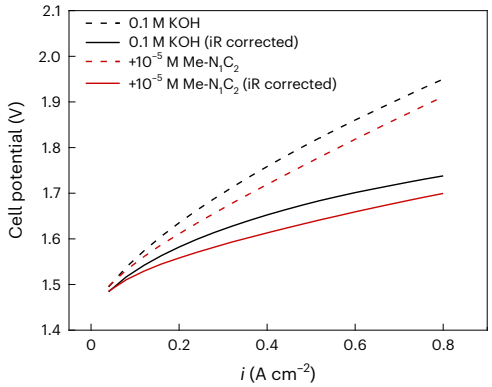

Fig. 6 | Me-N_1C_2 improves the AEMEL performance. AEMEL polarization curves with and without adding 10^{-5} M Me-N_1C_2 into the 0.1 M KOH solution fed into the cathode with and without iR correction. Cathode: 0.12 mg_{Pt} cm^{-2} Pt/C; anode: 3.1 mg_{IrOx} cm^{-2} IrO_x; membrane: PAP-TP-85-MQN-10C; 60 °C; electrode area 25 cm^2. The resistance with and without adding 10^{-5} M Me-N_1C_2 are 9.5 mΩ and 9.7 mΩ, respectively.

H_2O(H-down)^{2nd} bonded with Me-N_1C_2 (Fig. 4b). The H_2O(H-up)^{1st} holding the H_2O(H-down)^{2nd} close to the surface is a classic bilayer structure model (Fig. 5a) proposed for the electrified Pt–water interface[22,40]. We infer that this H_2O(H-down)^{2nd} can donate its H to the H_2O(H-up)^{1st} during the Volmer step, like the H_2O(H-down)^{2nd} bonded with Me-N_1C_2.

An alternative bilayer structure model is that the H_2O(H-up)^{1st} binding with the H_2O(H-down)^{1st} (Fig. 5b)[40]. The Volmer step based on this model in alkali (Fig. 5b, (i) → (iii)) was recently formulated[41]. By the formulation, the H_2O_{ad}(H-up) donates its H to the H_2O_{ad}(H-down) after its dissociation. This step is coupled with circulation of an electron from the Pt surface to the H_2O_{ad}(H-down), then H_2O_{ad}(H-up) and then back to the Pt surface as indicated by yellow arrows in Fig. 5b, (ii) (refs. 41,42). This OH_{ad} naturally forms an H-bond with the newly formed H_2O molecule above (Fig. 5b (iii)) and can therefore diffuse into the bulk electrolyte through it (Fig. 5b, (iii) → (iv). The reverse direction (Fig. 5b, (v) → (i)) describes the Volmer step of the HOR of Pt in alkali. The net result of the two consecutive processes (Fig. 5b, (ii) ↔ (iv)) are equivalent to the dissociation/formation of the H_2O_{ad}(H-down) via the proton-coupled electron transfer (PCET) process (Fig. 5b, (vi)), which leads to an apparent pathway of (i) ↔ (vi) ↔ (v) without explicitly involving OH_{ad}, as proposed recently[43,44].

In both models the H_2O(H-up)^{1st} catalyses diffusion of OH^- thereby promoting the Volmer step of Pt in alkali. Likewise, it catalyses diffusion of H^+ by the Grotthuss mechanism (Fig. 5c)[37]. We therefore infer that it facilitates the Volmer step of Pt in acid ($H_{ad} \leftrightarrow H^+ + e^-$) that is governed by diffusion of H^+ across the interface. As pH increases, the H_2O(H-up)^{1st} gets progressively destabilized and/or depopulated by the increasing repelling IEF, and the HER/HOR kinetics of Pt slows down. The diffusion rate of hydroxides in water is about half of that of protons[45], which may make minor contributions to the two orders of magnitude lower HER/HOR rates of Pt in alkali than in acid[3]. The major contribution comes from the pH-dependent interfacial water re-orientation that governs the H^+/OH^- diffusion[37,38,45]. By this argument, the sluggish HER/HOR of Pt in alkali can be promoted by surface Ru by stabilizing H_2O(H-up)^{1st} (Fig. 5d) as we proposed before[17], or by *N*-methylimidazoles that hold the H_2O(H-down)^{2nd} close to Pt surfaces like the H_2O(H-up)^{1st} (Fig. 5e).

Practical application

Reconstruction of interfacial H_2O also promotes HER/HOR kinetics of Pt in practical devices with alkaline media such as anion exchange membrane electrolysers (AEMELs), for which the repelling interfacial IEF is expected from the high pH environment. By adding 10^{-5} M Me-N_1C_2 into the 0.1 M KOH solution fed into the Pt/C cathode of an AEMEL (for details, see Methods), the iR-corrected current density at 1.6 V increased by ~40% (Fig. 6). This result demonstrates an alternative route to improve AEMEL performance by introducing organic compounds into the interface.

Conclusions

The Grotthuss mechanism governs proton and hydroxide diffusion through the H-bond network in bulk water. Here we showed that proton and hydroxide diffuse across the Pt–water interface through the H-bond network during the HER/HOR. The IEF at the electrified Pt–water interface frustrates the interfacial H-bond network by re-orientating interfacial water, thereby hindering the diffusion of protons and hydroxides across the interface and in turn the HER/HOR. Restoring the interfacial H-bond network resumes the HER/HOR kinetics.

Methods

Chemicals

Carbon support Pt (47.7%, TEC10V50E, TANAKA), iridium black (99.95% (metals basis), Alfa Aesar), potassium hydroxide (99.99%, Sigma-Aldrich), perchloric acid (70%, Sigma-Aldrich), isopropanol (ACS grade, Fisher Scientific), caffeine (99.7%, Alfa Aesar), 1,3-dimethyluracil (99%, Aldrich), imidazole (99%, Acros Organics), 1-methylimidazole (99%, Acros Organics), 2-methylimidazole (99%, Acros Organics), 4-methylimidazole (98%, Tokyo Chemical Industry), 2,4-dimethylimidazole (97%, Alfa Aesar), 1,2-dimethylimidazole (98%, Tokyo Chemical Industry), dichloromethane (99.9%, extra dry, Acros Organics), deuterium oxide (99.8% (Isotopic), Acros Organics), dichloromethane-d2 (99.9% (Isotopic), Alfa Aesar), argon (5.0, UN1006 Middlesex Gas) and hydrogen (UN1049, Middlesex Gas) were used as received. Ultrapure water (18.2 mΩ cm^{-1}) was prepared by the ultrapure water (Type I) Aqua Solutions system.

Electrochemical cell and electrolyte preparation

Electrochemical condition experiments in acid (0.1 M $HClO_4$) were conducted in a glass cell. The electrochemical measurements in alkaline solution (0.1 M KOH) were performed in a polytetrafluoroethylene (PTFE) cell. Before each measurement, all glassware and plastic jars were deep cleaned, then rinsed in ultrapure water at least six times. The electrolyte was prepared with ultrapure water and perchloric acid or potassium hydroxide. The glassy carbon electrode embedded in PTFE was used as the working electrode with a Pt mesh counter electrode and an RHE. The Pt mesh was sonicated in ultrapure water at least six times before being used.

Electrode preparation

Before drop-casting, the glassy carbon electrode (0.2463 cm^2) embedded in PTFE was polished mechanically with 0.5 mm, 0.3 mm, 0.05 mm alumina powder and then sonicated in ultrapure water and isopropanol at least three times. Each time took 5 min. Ink was freshly prepared each time with 2.4 mg 47.7% Pt/C, 2.55 ml ultrapure water, 0.51 ml isopropanol and 7.65 µl 5% Nafion. The ink was sonicated in the ice-water bath for 1 h before drop-casting. Each time 5.3 µl ink was used to drop-cast on the glassy carbon electrode with a rotation rate of 450 r.p.m. to achieve a Pt loading of 8 µg cm^{-2}. The electrode was dried in the air for about 30 min before use and rinsed with ultrapure water before electrochemical conditions.

Electrochemical measurements

All potentials reported in this work are referenced to the RHE. Before the RDE testing in 0.1 M KOH, the electrode was cycled in a stagnant Ar-saturated 0.1 M $HClO_4$ electrolyte with a scan rate of 500 mV s^{-1} within the potential range of 0.05–1.2 V for 100 cycles. The CV was performed in a stagnant Ar-saturated 0.1 M KOH at room temperature with a potential range of 0.05–1.0 V versus RHE at a scan rate of 20 mV s^{-1}. The HER/HOR polarization curves were obtained through

the potential cycling between −0.2 V and 0.9 V in an H_2-saturated 0.1 M KOH at room temperature with a rotation rate of 2,500 r.p.m. and a scan rate of 20 mV s^{-1}. All polarization curves in this work (Fig. 1 and Supplementary Figs. 1, 3 and 4) were normalized by the geometric surface area of the RDE electrode and iR-corrected. Experiments were repeated at least three times, and the averaged values were reported with standard deviations.

The HOR kinetic current densities, used for the calculation of exchange current densities, were calculated using the Koutecky–Levich equation (equation (1)) to adjust for mass transport limitations.

$$\frac{1}{i} = \frac{1}{i_d} + \frac{1}{i_k} \quad (1)$$

where i is the as-measured current density, i_d is the diffusion-limited current density and i_k is the kinetic current density. The exchange current density (i_0) was calculated on the basis of the Butler–Volmer equation (equation (2)), by multiplying the slope of the lines of the micropolarization regions (η = ±10 mV). The value of ($\alpha_a + \alpha_b$) is approximately assumed to be 1.

$$i_0 (\alpha_a + \alpha_b) = \frac{RTi_\eta}{F\eta}, \quad (2)$$

where α_a and α_b are anodic and cathodic transfer coefficients; F is Faraday's constant; R is the ideal gas constant; and T is temperature.

Electrochemical impedance spectroscopy measurements were measured with frequencies from 10^5 to 0.1 Hz with an amplitude of 10 mV by using Autolab Potentiostat.

Electrochemical deposition of *N*-methylimidazoles

After CV and HER/HOR measurements, the *N*-methylimidazole was added into 0.1 M KOH to reach a concentration of 10^{-5} M. Then, the polarization curve and the CV were recorded in an H_2 or Ar-saturated 0.1 M KOH electrolyte, respectively, using the same procedure as described above. Each measurement was conducted at least three times, and the averaged values were reported with standard deviations.

CO stripping

Two potential cycles between 0.05 V and 1 V in an Ar-saturated 0.1 M KOH were applied to the electrode at the scan rate of 20 mV s^{-1} before the adsorption of carbon monoxide by purging 1% CO at a constant potential of 0.05 V for 15 min into the electrolyte. Then Ar was purged into the same electrolyte for 25 min at the same potential to remove the CO from the electrolyte. Then two potential cycles between 0.05 V and 1.0 V at a scan rate of 20 mV s^{-1} were recorded.

AEMEL testing

Carbon cloth loaded with carbon and PTFE prepared by Advent Technologies was used as the gas diffusion layer for the cathode, and porous titanium plate (Nel) was used as the anode. The electrode area was 25 cm^2. Prepared by our group at University of Delaware, 11% PAP-TP-85 in ethanol was used as ionomer, and PAP-TP-85-MQN-10C from the same group with a thickness of 20 μm was used as the membrane.

For the preparation of the cathode, the Pt/C catalyst (47.7%, TKK) and PAP-TP-85 solution were sonicated with ultrapure water and isopropanol in an ice-water bath for 2 h to obtain a well-dispersed catalyst ink. The catalyst ink was then hand-sprayed on the carbon cloth using the spray gun (iwata, HP-CS) to achieve a Pt loading of 0.12 mg cm^{-2} and ionomer loading of 25% versus catalyst. A low loading of Pt was used in the cathode here to render the HER kinetics as the limiting factor of the AEMEL performance. For the preparation of the anode, IrO_x and PAP-TP-85 solution were sonicated with ultrapure water and isopropanol in an ice-water bath for 2 h to obtain a well-dispersed catalyst ink. The catalyst ink was then hand-sprayed on the carbon cloth using the spray gun (iwata, HP-CS) to reach an IrO_x loading of 3.1 mg cm^{-2} and ionomer loading of 10% versus catalyst.

The AEMEL performance was tested using a homemade water electrolysis setup. Two litres of 0.1 M KOH were fed into the anode at a flow rate of 250 ml min^{-1} and cathode at a flow rate of 200 ml min^{-1}, respectively. Hewlett Packard 6651A System DC power supply was used to provide the voltage and current necessary for the water-splitting reaction. Keysight 34461A digit multimeter was used to precisely collect current and voltage for the polarization curve. The activation of the cell was first carried out at 0.1 A cm^{-2} for 5 min and 0.2 A cm^{-2} for 30 min. The polarization curve was then recorded at 60 °C by stepping the current density from 0.04 to 0.8 A cm^{-2} with an increment of 0.04 A cm^{-2}, and each current density was held for 3 min, and the data of the last 30 s were averaged and used as the reported value. After the measurement, 0.1 M KOH at both anode and cathode were replaced as fresh one, and Me-N_1C_2 was added into 0.1 M KOH at the cathode to achieve a concentration of 10^{-5} M. The same procedure was then repeated to collect the polarization curve.

Electrochemical impedance spectroscopy measurements were performed with frequencies from 10^5 to 0.1 Hz with an amplitude of 10 mV by using Autolab Potentiostat.

NMR measurement

All NMR experiments were performed on a Bruker AVANCE II 400 MHz NMR spectrometer using a BBFO probe equipped with *z*-axis gradient. The ^{14}N-spectra of imidazole, Me-N_1, Me-C_2, Me-N_1C_2 and ^{15}N- spectra of imidazole, Me-N_1, Me-C_4 and Me-$C_{2,4}$ in either 0.1 M KOH solution (90%/10% H_2O/D_2O) or 90%/10% CH_2Cl_2/CD_2Cl_2 were recorded with proton decoupling during data acquisition. For the ^{15}N-experiments, a 2 mM $Cr(acac)_3$ was added to each sample to reduce the relaxation times. The chemical shift scales were referenced as outlined in the IUPAC Recommendations of 2001 (ref. 46). Specifically, the ^{14}N- and ^{15}N- chemical shifts are reported relative to liquid ammonium using nitromethane in chloroform (10% v/v) and 1 M $^{15}NH_4Cl$ aqueous solution as external reference, respectively.

XAS measurement

A Pt/C catalyst (47.7%, TKK) and Nafion were sonicated with ultrapure water and isopropanol in an ice-water bath for 1 h to obtain a well-dispersed catalyst ink. The catalyst ink was then hand-sprayed on the carbon paper using the spray gun (iwata, HP-CS) to achieve a Pt loading of 0.2 mg cm^{-2} with an ionomer-to-carbon weight ratio of 0.4.

The prepared electrode was cut into 1.5 × 1.5 cm^2 square and conducted an acid condition process with a scan rate of 50 mV s^{-1} from 0.05 V to 0.95 V for 100 cycles in an Ar-saturated 0.1 M $HClO_4$. After that, CV was collected in 0.1 M KOH with a scan rate of 20 mV s^{-1} from 0.05 V to 0.90 V in an Ar-saturated 0.1 M KOH. Me-N_1C_2 was then added into 0.1 M KOH to reach a concentration of 10^{-5} M. Potential cycling from 0.05 V to 0.90 V was then applied with a scan rate of 50 mV s^{-1} until the CV became stable. Another CV was collected to verify the successful deposition of Me-N_1C_2 on the surface of the electrode by using the same procedure as previously described.

XAS data were collected at the Pt L_3-edge, for both Pt/C electrodes with and without Me-N_1C_2 for comparison, in fluorescence mode at beamline 7-BM of the National Synchrotron Light Source II at Brookhaven National Laboratory, NY. A full range of XAS (0–15 $Å^{-1}$ in the *K* space), including both the extended X-ray absorption fine structure and X-ray absorption near-edge structure spectra, were collected. Each measurement was conducted for at least ten scans that were later averaged to improve the signal-to-noise ratio.

In situ ATR-SEIRAS

The ATR-SEIRAS experiments were performed in a custom spectro-electrochemical cell with the Si crystal reflecting plane mounted on the side. The chemically deposited polycrystalline Pt film on the prism

served as the working electrode, with a graphite rod counter. These were separated with a Nafion membrane to prevent contamination of the Pt surface. An Ag/AgCl (3.0 M KCl, BASi) reference electrode was used for all experiments. Electrolytes were purified through electrolysis by holding an Au working electrode at a constant negative current, allowing for deposition of metal impurities on the Au electrode. All spectroscopic measurements were collected with 4 cm^{-1} resolution and at least 64 co-added scans using an Agilent Technologies Cary 660 FTIR spectrometer equipped with a liquid-nitrogen-cooled mercury cadmium telluride detector. Electrochemical measurements were conducted using a Solartron SI 1260/1287 system. Impedance measurements were conducted at the beginning of each experiment, and the internal resistance (typically 40–90 Ω) was actively corrected for throughout all experiments. Spectra are presented in absorbance, with positive peaks signifying an increase and negative representing a decrease in interfacial species.

In situ surface-enhanced Raman

The in situ Raman experiments were performed in a custom spectroelectrochemical cell. The polycrystalline Ag film deposited on the glassy carbon served as the working electrode, with a Pt wire as counter electrode. An Ag/AgCl (saturated KCl) reference electrode was used for all experiments. The working and counter electrodes were separated with a Nafion membrane to avoid contamination. The 0.1 M KOH electrolytes were purified as depicted in the in situ ATR-SEIRAS experiment. All spectroscopic measurements were carried out using a Raman spectrometer (HORIBA, LabRAM HR Evolution) equipped with an Olympus objective lens (LUMFL, 60×, numerical aperture: 1.10). The excitation wavelength was a visible light laser (532 nm). Electrochemical measurements were conducted using an Ivium (CompactStat) electrochemical workstation, and the current was stabilized for about 5 min at each potential before the Raman spectra were collected.

DFT calculations

The DFT calculations were performed using the Gaussian 16 program[47]. The imidazole, Me-N_1, Me-C_2, Me-C_4, Me-C_5, Me-N_1C_2, Me-$C_{2,4}$ and Me-$C_{2,5}$ were optimized using hybrid density functional PBE0 (ref. 48)–GD3BJ (ref. 49) with the aug-cc-pVTZ (ref. 50) basis set with the integral equation formalism variant of the polarizable continuum model[51] with parameters for water. We performed a vibrational analysis to confirm that each stationary point is a minimum (only positive vibrational frequencies). A natural bond orbital analysis[52] was performed to provide the atomic partial charges.

For imidazole, Me-C_2, Me-C_4 and Me-$C_{2,4}$, the rapid averaging of N_1 and N_3 charge via proton exchange (that is, the proton is instantaneously shared by N_1 and N_3) that occurs at aqueous solution with pH >10 (ref. 20) was taken under consideration to determine the charge of N_3. Detailed calculations are given in Supplementary Note 1.

AIMD calculations

To obtain a well-equilibrated water structure on Pt surface for AIMD simulations, we first simulated the water–Pt(100) interface using 60 explicit water molecules on a 4 × 4 Pt(100) surface slab (three layers) with an area of 1.23 nm^2 and a height of 40 Å along the z axis. To equilibrate the waters interacting with the interface, we carried out 2 ns of reactive molecular dynamics simulations with 0.25 fs timestep using the reactive force field for Pt and 60 H_2O (ref. 53). The reactive force field molecular dynamics simulation was carried out using Largescale Atomic/Molecular Massively Parallel Simulator[54] with user package of Reax/C (ref. 55). Canonical ensemble (NVT) simulations with a fixed number of atoms, N, a fixed volume, V, and a fixed temperature, T, were performed with a timestep of 0.25 fs, using the Nose–Hoover thermostat[56] at 298 K with a damping parameter of 100 fs.

Starting from the geometry with fully connected H-bond network, we removed 3 H_2O and added a target organic molecule. Then, we carried out ab initio AIMD simulation at 298 K for 30 ps to 70 ps for the system to reach equilibrium. Our AIMD simulations used the Vienna ab initio simulation package (VASP ver. 5.4.5)[57,58] with the VASPsol solvation model[59]. Electron exchange and correlation were treated within the generalized gradient approximation[60] in the form of the PBE functional, including the D3 correction for London dispersion (van der Waals attraction)[61]. The interaction between the ionic core and the valence electrons was described by the projector-augmented wave method[62]. We used a plane-wave basis set with an energy cut-off of 400 eV. The convergence criteria for the electronic structure was 10^{-5} eV. Only the top surface Pt was allowed to move, with the sublayers fixed to the bulk lattice parameters. The Brillouin zone was only sampled at gamma point of Brillouin zone without any symmetry. The hydrogen mass of water is set to 2 atomic mass units (D_2O) for a more accurate description of water in classical dynamics. The Nose–Hoover thermostat was applied to keep the temperature at 298 K using a temperature damping parameter of 100 fs. The velocities were rescaled every 20 steps to re-adjust the target temperature to equilibrium.

To obtain the kinetic barrier of the Volmer step, a metadynamics simulation was performed using the last atomic configurations and velocities from the equilibration. The CV was defined as the difference between two atomic distances: $CV = d_{Pt\text{-}H} - d_{O\text{-}H}$, where $d_{Pt\text{-}H}$ is the distance between the surface Pt atom and the H atom of the interfacial water, and $d_{O\text{-}H}$ is the bond length of the water. This variable induces proton transfer from interfacial water to the Pt surface. The starting structures including the atomic configurations and velocities and predictor–corrector coordinates for the two systems, $60H_2O$/Pt and Me-N_1C_2*/$57H_2O$/Pt (parallel) (Supplementary Fig. 11) are provided as Supplementary Data 1 and 2, respectively. A time-dependent bias potential was applied with 20 fs time intervals with Gaussian height (h) of 0.08 eV and width (w) of 0.18 eV. To prevent the water diffusion from the interface to bulk water without Volmer reaction, a single Gaussian hill with h = 1.0 eV and w = 0.2 eV is applied to guide the metadynamics not to exceed a CV of 2 Å. After the barrier crossing, the kinetic barrier was then calculated by summing the Gaussian potential. The deposition history of Gaussian potential with and without Me-N_1C_2 are provided in Supplementary Data 3 and 4, respectively. The time evolution of CV and potential energy landscape as a function of CV with and without Me-N_1C_2 (Supplementary Data 5 and 6) are displayed in Supplementary Fig. 15 with the raw data given in Supplementary Data 7.

Data availability

The data supporting the findings of this study are available within this article and its Supplementary Information. Additional data are available from the corresponding authors upon reasonable request. Source data are provided with this paper.

References

1. Sheng, W. et al. Correlating hydrogen oxidation and evolution activity on platinum at different pH with measured hydrogen binding energy. *Nat. Commun.* **6**, 5848 (2015).
2. Zheng, J., Sheng, W., Zhuang, Z., Xu, B. & Yan, Y. Universal dependence of hydrogen oxidation and evolution reaction activity of platinum-group metals on pH and hydrogen binding energy. *Sci. Adv.* **2**, e1501602 (2016).
3. Durst, J. et al. New insights into the electrochemical hydrogen oxidation and evolution reaction mechanism. *Energy Environ. Sci.* **7**, 2255–2260 (2014).
4. McCrum, I. T. & Koper, M. T. M. The role of adsorbed hydroxide in hydrogen evolution reaction kinetics on modified platinum. *Nat. Energy* **5**, 891–899 (2020).
5. Liu, E. et al. Unifying the hydrogen evolution and oxidation reactions kinetics in base by identifying the catalytic roles of hydroxyl-water-cation adducts. *J. Am. Chem. Soc.* **141**, 3232–3239 (2019).

6. Li, J. et al. Experimental poof of the bifunctional mechanism for the hydrogen oxidation in alkaline media. *Angew. Chem. Int. Ed.* **56**, 15594–15598 (2017).
7. Strmcnik, D. et al. Improving the hydrogen oxidation reaction rate by promotion of hydroxyl adsorption. *Nat. Chem.* **5**, 300–306 (2013).
8. Schwämmlein, J. N. et al. Origin of superior HOR/HER activity of bimetallic Pt-Ru catalysts in alkaline media identified via Ru@Pt core-shell nanoparticles. *J. Electrochem. Soc.* **165**, H229–H239 (2018).
9. Wang, Y. et al. Pt–Ru catalyzed hydrogen oxidation in alkaline media: oxophilic effect or electronic effect? *Energy Environ. Sci.* **8**, 177–181 (2015).
10. Lu, S. & Zhuang, Z. Investigating the influences of the adsorbed species on catalytic activity for hydrogen oxidation reaction in alkaline electrolyte. *J. Am. Chem. Soc.* **139**, 5156–5163 (2017).
11. Elbert, K. et al. Elucidating hydrogen oxidation/evolution kinetics in base and acid by enhanced activities at the optimized Pt shell thickness on the Ru core. *ACS Catal.* **5**, 6764–6772 (2015).
12. Ledezma-Yanez, I. et al. Interfacial water reorganization as a pH-dependent descriptor of the hydrogen evolution rate on platinum electrodes. *Nat. Energy* **2**, 17031 (2017).
13. Intikhab, S. et al. Exploiting dynamic water structure and structural sensitivity for nanoscale electrocatalyst design. *Nano Energy* **64**, 103963 (2019).
14. Briega-Martos, V., Ferre-Vilaplana, A., Herrero, E. & Feliu, J. M. Why the activity of the hydrogen oxidation reaction on platinum decreases as pH increases. *Electrochim. Acta* **354**, 136620 (2020).
15. Rebollar, L. et al. "Beyond adsorption" descriptors in hydrogen electrocatalysis. *ACS Catal.* **10**, 14747–14762 (2020).
16. Rebollar, L. et al. On the relationship between potential of zero charge and solvent dynamics in the reversible hydrogen electrode. *J. Catal.* **398**, 161–170 (2021).
17. Liu, E. et al. Interfacial water shuffling the intermediates of hydrogen oxidation and evolution reactions in aqueous media. *Energy Environ. Sci.* **13**, 3064–3074 (2020).
18. Intikhab, S. et al. Caffeinated interfaces enhance alkaline hydrogen electrocatalysis. *ACS Catal.* **10**, 6798–6802 (2020).
19. Sheng, W., Gasteiger, H. A. & Shao-Horn, Y. Hydrogen oxidation and evolution reaction kinetics on platinum: acid vs alkaline electrolytes. *J. Electrochem. Soc.* **157**, B1529–B1536 (2010).
20. Alei, M. & Wageman, W. E. ^{15}N NMR shifts for imidazole and 1-methyl imidazole in CH_2Cl_2 relative to aqueous solution. *Tetrahedron Lett.* **20**, 667–670 (1979).
21. Zischang, J., Lee, J. J. & Suhm, M. A. Communication: where does the first water molecule go in imidazole? *J. Chem. Phys.* **135**, 061102 (2011).
22. Osawa, M., Tsushima, M., Mogami, H., Samjeské, G. & Yamakata, A. Structure of water at the electrified platinum–water interface: a study by surface-enhanced infrared absorption spectroscopy. *J. Phys. Chem. C* **112**, 4248–4256 (2008).
23. Ataka, K.-i, Yotsuyanagi, T. & Osawa, M. Potential-dependent reorientation of water molecules at an electrode/electrolyte interface studied by surface-enhanced infrared absorption spectroscopy. *J. Phys. Chem.* **100**, 10664–10672 (1996).
24. Yao, Y., Zhu, S., Wang, H., Li, H. & Shao, M. A spectroscopic study on the nitrogen electrochemical reduction reaction on gold and platinum surfaces. *J. Am. Chem. Soc.* **140**, 1496–1501 (2018).
25. Li, C.-Y. et al. In situ probing electrified interfacial water structures at atomically flat surfaces. *Nat. Mater.* **18**, 697–701 (2019).
26. Toney, M. F. et al. Voltage-dependent ordering of water molecules at an electrode–electrolyte interface. *Nature* **368**, 444–446 (1994).
27. Nagy, G. & Heinzinger, K. A molecular dynamics study of water monolayers on charged platinum walls. *J. Electroanal. Chem.* **327**, 25–30 (1992).
28. Wang, S.-H. & Griffiths, P. R. Resolution enhancement of diffuse reflectance i.r. spectra of coals by Fourier self-deconvolution: 1. C–H stretching and bending modes. *Fuel* **64**, 229–236 (1985).
29. Lambert, D. K. Vibrational stark effect of adsorbates at electrochemical interfaces. *Electrochim. Acta* **41**, 623–630 (1996).
30. Teliska, M., O'Grady, W. E. & Ramaker, D. E. Determination of H adsorption sites on Pt/C electrodes in $HClO_4$ from Pt L_{23} X-ray absorption spectroscopy. *J. Phys. Chem. B* **108**, 2333–2344 (2004).
31. Roth, C. et al. Determination of O[H] and CO coverage and adsorption sites on PtRu electrodes in an operating PEM fuel cell. *J. Am. Chem. Soc.* **127**, 14607–14615 (2005).
32. Maniguet, S., Mathew, R. J. & Russell, A. E. EXAFS of carbon monoxide oxidation on supported Pt fuel cell electrocatalysts. *J. Phys. Chem. B* **104**, 1998–2004 (2000).
33. Carter, D. A., Pemberton, J. E. & Woelfel, K. J. Orientation of 1- and 2-methylimidazole on silver electrodes determined with surface-enhanced Raman scattering. *J. Phys. Chem. B* **102**, 9870–9880 (1998).
34. Papoian, G., Nørskov, J. K. & Hoffmann, R. A comparative theoretical study of the hydrogen, methyl, and ethyl chemisorption on the Pt(111) surface. *J. Am. Chem. Soc.* **122**, 4129–4144 (2000).
35. Cheng, T., Wang, L., Merinov, B. V. & Goddard, W. A. Explanation of dramatic pH-dependence of hydrogen binding on noble metal electrode: greatly weakened water adsorption at high pH. *J. Am. Chem. Soc.* **140**, 7787–7790 (2018).
36. Laio, A. & Parrinello, M. Escaping free-energy minima. *Proc. Natl Acad. Sci. USA* **99**, 12562–12566 (2002).
37. Marx, D., Tuckerman, M. E., Hutter, J. & Parrinello, M. The nature of the hydrated excess proton in water. *Nature* **397**, 601–604 (1999).
38. Tuckerman, M. E., Marx, D. & Parrinello, M. The nature and transport mechanism of hydrated hydroxide ions in aqueous solution. *Nature* **417**, 925–929 (2002).
39. Dunnington, B. D. & Schmidt, J. R. Generalization of natural bond orbital analysis to periodic systems: applications to solids and surfaces via plane-wave density functional theory. *J. Chem. Theory Comput.* **8**, 1902–1911 (2012).
40. Ogasawara, H. et al. Structure and bonding of water on Pt(111). *Phys. Rev. Lett.* **89**, 276102 (2002).
41. Lam, Y.-C., Soudackov, A. V., Goldsmith, Z. K. & Hammes-Schiffer, S. Theory of proton discharge on metal electrodes: electronically adiabatic model. *J. Phys. Chem. C* **123**, 12335–12345 (2019).
42. Meng, S., Wang, E. G. & Gao, S. Water adsorption on metal surfaces: a general picture from density functional theory studies. *Phys. Rev. B* **69**, 195404 (2004).
43. Rebollar, L., Intikhab, S., Snyder, J. D. & Tang, M. H. Determining the viability of hydroxide-mediated bifunctional HER/HOR mechanisms through single-crystal voltammetry and microkinetic modeling. *J. Electrochem. Soc.* **165**, J3209–J3221 (2018).
44. Intikhab, S., Snyder, J. D. & Tang, M. H. Adsorbed hydroxide does not participate in the volmer step of alkaline hydrogen electrocatalysis. *ACS Catal.* **7**, 8314–8319 (2017).
45. Chen, M. et al. Hydroxide diffuses slower than hydronium in water because its solvated structure inhibits correlated proton transfer. *Nat. Chem.* **10**, 413–419 (2018).
46. Harris, R. K., Becker, E. D., De Menezes, S. M. C., Goodfellow, R. & Granger, P. NMR nomenclature. Nuclear spin properties and conventions for chemical shifts (IUPAC Recommendations 2001). *Pure Appl. Chem.* **73**, 1795–1818 (2001).
47. Gaussian 16 Rev. C.01 (Wallingford CT, 2016).
48. Adamo, C. & Barone, V. Toward reliable density functional methods without adjustable parameters: the PBE0 model. *J. Chem. Phys.* **110**, 6158–6170 (1999).

49. Grimme, S., Ehrlich, S. & Goerigk, L. Effect of the damping function in dispersion corrected density functional theory. *J. Comput. Chem.* **32**, 1456–1465 (2011).
50. Woon, D. E. & Dunning, T. H. Jr. Gaussian basis sets for use in correlated molecular calculations. V. Core-valence basis sets for boron through neon. *J. Chem. Phys.* **103**, 4572–4585 (1995).
51. Tomasi, J., Mennucci, B. & Cancès, E. The IEF version of the PCM solvation method: an overview of a new method addressed to study molecular solutes at the QM ab initio level. *J. Mol. Struct. THEOCHEM* **464**, 211–226 (1999).
52. Dunnington, B. D., Schmidt, J. R., Dunnington, B. D. & Schmidt, J. R. Generalization of natural bond orbital analysis to periodic systems: applications to solids and surfaces via plane-wave density functional theory. *J. Chem. Theory Comput.* **8**, 1902–1911 (2012).
53. Shin, Y. K., Gai, L., Raman, S. & van Duin, A. C. T. Development of a ReaxFF reactive force field for the Pt–Ni alloy catalyst. *J. Phys. Chem. A* **120**, 8044–8055 (2016).
54. Plimpton, S. Fast parallel algorithms for short-range molecular dynamics. *J. Comput. Phys.* **117**, 1–19 (1995).
55. Aktulga, H. M., Fogarty, J. C., Pandit, S. A. & Grama, A. Y. Parallel reactive molecular dynamics: numerical methods and algorithmic techniques. *Parallel Comput.* **38**, 245–259 (2012).
56. Shuichi, N. Constant temperature molecular dynamics methods. *Prog. Theor. Phys.* **103**, 1–46 (1991).
57. Kresse, G. & Hafner, J. Ab initio molecular-dynamics simulation of the liquid-metal–amorphous-semiconductor transition in germanium. *Phys. Rev. B* **49**, 14251–14269 (1994).
58. Kresse, G. & Furthmüller, J. Efficient iterative schemes for ab initio total-energy calculations using a plane-wave basis set. *Phys. Rev. B* **54**, 11169–11186 (1996).
59. Mathew, K., Sundararaman, R., Letchworth-Weaver, K., Arias, T. A. & Hennig, R. G. Implicit solvation model for density-functional study of nanocrystal surfaces and reaction pathways. *J. Chem. Phys.* **140**, 084106 (2014).
60. Perdew, J. P., Burke, K. & Ernzerhof, M. Generalized gradient approximation made simple. *Phys. Rev. Lett.* **77**, 3865–3868 (1996).
61. Johnson, E. R. & Becke, A. D. A post-Hartree–Fock model of intermolecular interactions: inclusion of higher-order corrections. *J. Chem. Phys.* **124**, 174104 (2006).
62. Blöchl, P. E. Projector augmented-wave method. *Phys. Rev. B* **50**, 17953–17979 (1994).

Acknowledgements

This work was supported by the Office of Naval Research (ONR) grant N000141712608 (Q.J.). This research used beamline 7-BM (QAS) of the National Synchrotron Light Source II, a US Department of Energy (DOE) Office of Science User Facility operated for the DOE Office of Science by Brookhaven National Laboratory Contract DE-SC0012704. Beamline operations were supported in part by the Synchrotron Catalysis Consortium Grant DE-SC0012335. W.A.G. acknowledges support by the Liquid Sunlight Alliance, which is supported by the US DOE, Office of Science, Office of Basic Energy Sciences, Fuels from Sunlight Hub under award number DE-SC0021266. This work used the Extreme Science and Engineering Discovery Environment (XSEDE) for AIMD simulation, which is supported by the NSF grant number ACI-1548562. S.K. acknowledges support from the Resnick Sustainability Institute at Caltech.

Author contributions

Q.J. conceived the project, designed the experiments and proposed the HER/HOR mechanism. Q.S. conducted the electrochemical experiments and the data analysis in S.M.'s lab partly under his supervision. S.T. and J.J.G. conducted the NMR experiments and analysed the data. Q.S. helped to prepare the NMR samples. S.K. and W.A.G. planned the AIMD calculations. N.M. and S.A.L. performed the DFT calculations and contributed to the writing of the DFT computational results. Y.Y. and N.J.O. conducted the in situ ATR-SEIRAS and data analysis. Y.Y. and N.J.O. repeated electrochemical RDE experiments. Q.S., L.M. and S.N.E. conducted the XAS experiments, and Q.J. did the data analysis. J.L. conducted the in situ surface-enhanced Raman and data analysis. Q.S. and I.K. conducted the AEMEL testing and analysed the data. Q.J. supervised the project and data analysis. Q.J., Y.Y., W.A.G., Q.S., N.J.O. and S.K. wrote the paper and prepared the figures.

Competing interests

The authors declare no competing interests.

Additional information

Supplementary information The online version contains supplementary material available at https://doi.org/10.1038/s41560-023-01302-y.

Correspondence and requests for materials should be addressed to Jingkun Li, William A. Goddard, Yushan Yan or Qingying Jia.

Peer review information *Nature Energy* thanks Batyr Garlyyev, Zhenhua Zeng and the other, anonymous, reviewer(s) for their contribution to the peer review of this work.